Zinc-Imidazolate Films as an All-Dry Resist Technology

*Peter Corkery [1, †], Kayley E. Waltz [1, †], Patrick M. Eckhert [2, †], Mueed Ahmad [3, 4], Andrea Kraetz [1], Yurun Miao [1], Dennis T. Lee [1, 4], Mohammed K. Abdel-Rahman [2], Yucheng Lan [6], Paul Haghi-Ashtiani [6], Aaron Stein [3], J. Anibal Boscoboinik [3, 4], Michael Tsapatsis [1, 5, *] & D. Howard Fairbrother [2, *]*

[1] Department of Chemical and Biomolecular Engineering & Institute for NanoBioTechnology, Johns Hopkins University, Baltimore, Maryland 21218, USA. E-mail: tsapatsis@jhu.edu

[2] Department of Chemistry, Johns Hopkins University, Baltimore, Maryland 21218, USA. E-mail: howardf@jhu.edu

[3] Center for Functional Nanomaterials, Brookhaven National Laboratory, Upton, New York 11973, USA

[4] Department of Materials Science and Chemical Engineering, Stony Brook University, Stony Brook, New York 11790, USA

[5] Applied Physics Laboratory, Johns Hopkins University, Laurel, Maryland 20723, USA

[6] Department of Physics and Engineering Physics, Morgan State University, Baltimore, Maryland 21251, USA

† These authors contributed equally to this work.

Keywords
Molecular layer deposition, dry development, dry etching, solvent-free, electron beam lithography, electron beam resist, high-resolution patterning

Abstract
Motivated by the drawbacks of solution phase processing, an all-dry resist formation process is presented that utilizes amorphous zinc-imidazolate (aZnMIm) films deposited by atomic/molecular layer deposition (ALD/MLD), patterned with electron beam lithography (EBL), and developed by novel low temperature (120 °C) gas phase etching using 1,1,1,5,5,5-hexafluoroacetylacetone (hfacH) to achieve well-resolved 22 nm lines with a pitch of 30 nm. The effects of electron beam irradiation on the chemical structure and hfacH etch resistance of aZnMIm films are investigated, and it is found that electron irradiation degrades the 2-methylimidazolate ligands and transforms aZnMIm into a more dense material that is resistant to etching by hfacH and has a C:N:Zn ratio effectively identical to that of unmodified aZnMIm. These findings showcase the potential for aZnMIm films to function in a dry resist technology. Sensitivity, contrast, and critical dimensions of the patterns are determined to be 37 mC cm^{-2}, 0.87, and 29 nm, respectively, for aZnMIm deposited on silicon substrates and patterned at 30 keV. This work introduces a new direction for solvent-free resist processing, offering the prospect of scalable, high-resolution patterning techniques for advanced semiconductor fabrication processes.

Introduction

Lithography, a principal technique in the fabrication of microelectronic devices, uses a thin sacrificial layer, called a resist, to transfer circuit patterns to the surface of a semiconductor substrate. Localized chemical reactions initiated within irradiated areas of the resist lead to differences in material properties, typically

solubility, compared to the unexposed areas that can be exploited in the subsequent development step to produce a pattern [1-2]. As microelectronic device dimensions continue to shrink, the push towards smaller-sized features remains a challenge and has led to the formation of nanometer scale patterns using state-of-the-art extreme ultraviolet lithography (EUVL) and direct-write electron beam (e-beam) lithography (EBL).

Spin-coating, the most common resist film deposition technique, necessitates a pre-bake step to remove excess solvent and leads to the production of precursor and organic solvent wastes that require additional chemical treatment. Dry deposition techniques, like chemical vapor deposition (CVD) and atomic/molecular layer deposition (ALD/MLD), offer potential advantages including a reduction in generated waste, elimination of adhesion or stability additives, and elimination of the pre-bake step following spin-coating [3-4]. Motivated by these potential advantages, solvent-free methods have already been used for uniformly depositing thin films of metal-organic frameworks (MOFs) and other organic-inorganic hybrid materials [5-12]. In a recent study, the feasibility of MLD-grown resists was demonstrated; amorphous MLD films consisting of hafnium and ethylene glycol were patterned with deep-ultraviolet and e-beam lithography to achieve features as small as 50 nm [13].

Following patterning, resists are typically developed using an organic solvent in a liquid phase processing step. There are, however, significant issues with this wet chemistry approach including solvent storage and disposal and limited feature resolution due to pattern collapse resulting from capillary forces during solvent evaporation [14]. To circumvent this limitation, interest has turned towards solvent-free "dry" etching techniques, typically involving reactive ion etching (RIE) using an oxygen or halogen plasma. The downside of RIE is the requirement for a high etch resistance of the remaining photoresist and the other materials present in the microelectronic device [15]. β-diketone compounds such as acetylacetone (acac) and 1,1,1,5,5,5-hexafluoroacetylacetone (hfacH) have been used for the chemical etching of various metal oxides [16-17] and in principle could offer an alternative to plasma-based etchants for organic-inorganic hybrid materials. Despite the drawbacks of liquid phase deposition and development and plasma-based etching, we are not aware of any peer-reviewed literature demonstrating nanoscale feature patterning using non-plasma-based dry processing for electron or photon-based lithography. Reports and patents from LAM Corporation on this topic will be discussed at the end of this manuscript [3-4, 18-19].

Driven by low photon fluxes, a new class of EUVL resist materials have emerged containing metals such as Zn, Hf, and Sn which have much higher EUV (13.5 nm, 92 eV) absorption cross sections than the elements in traditional polymer-based resists [4, 13, 18-20]. Zeolitic imidazolate frameworks (ZIFs), a class of MOFs studied for a variety of applications including gas separations and sensing, microelectronics, and catalysis [21-25], have been reported to be e-beam patternable [26]. More recently, this potential has been further developed in several studies [22, 25, 27-30]. Specifically, patterning studies of *polycrystalline* ZIF films have used e-beam irradiation for bottom-up patterning via a two-step patterned-growth CVD process [28] or top-down patterning via e-beam and x-ray irradiation of CVD ZIF films followed by solution phase development [22], to produce line features as small as 60 nm. In these patterned crystalline films, the presence, growth, and reformation of discrete crystal domains have led to increased line edge roughness (LER) and limited resolution. In contrast, an *amorphous* spin-coated film consisting of zinc-containing inorganic-organic clusters yielded lines with a half-pitch as low as 13 nm following EUV exposure and solution phase development [20]. More recently, e-beam patterning of amorphous ZIF films formed via a liquid phase (dip-coating) deposition process and solution phase development produced well-resolved line features at a half-pitch of 20 nm [30]. Another benefit of using metal-containing resist materials, specifically as etch masks, is their increased etch resistance when compared to conventional polymer resists. In a recent study, a Cr-containing metal-organic resist demonstrated an Si etch selectivity of nearly 100:1 [31], while

ZEP520A, a typical organic photoresist, had an etch selectivity of approximately 1:1 for similar etch conditions [32].

In this work, we demonstrate an all-dry resist process wherein amorphous zinc-2-methylimidazolate (aZnMIm) thin films deposited via ALD/MLD are patterned with EBL and developed with a vapor phase β-diketone etchant. The use of β-diketones for the vapor phase synthesis [33-34] and post synthetic modification [35] of MOFs has been demonstrated in the literature; however, their use for the dry development of patterned MOFs or other organic-inorganic hybrid materials has not previously been demonstrated. We show that this solvent-free deposition and etching process achieves feature sizes as small as 22 nm. This new process combines the potential advantages of increased throughput and economical precursor usage associated with dry deposition methods with the improved line resolution of amorphous thin films. Moreover, it could be more resistant to pattern collapse and other mechanical stress failure issues associated with solution phase development.

We first present our ALD/MLD method to deposit smooth and continuous aZnMIm films which have composition and bonding, as probed by X-ray photoelectron (XPS) and vibrational spectroscopy (infrared reflection absorption spectroscopy - IRRAS), similar to crystalline ZIFs but lack long range crystalline order, as shown by X-ray diffraction (XRD). These results are contrasted with a recent report [7] on the deposition of amorphous and crystalline ZIF films. We then demonstrate that e-beam irradiation, while preserving the C:N:Zn ratio of the aZnMIm, leads to moderate densification and drastic chemical changes within the aZnMIm film, which render it resistant to etching upon exposure to hfacH, while the non-irradiated aZnMIm is readily and completely etched by hfacH. These observations set the stage for the introduction of a high-resolution negative tone dry patterning method using aZnMIm resists, which is described in the final section of this paper along with a comparison to other recent reports on all-dry patterning methods.

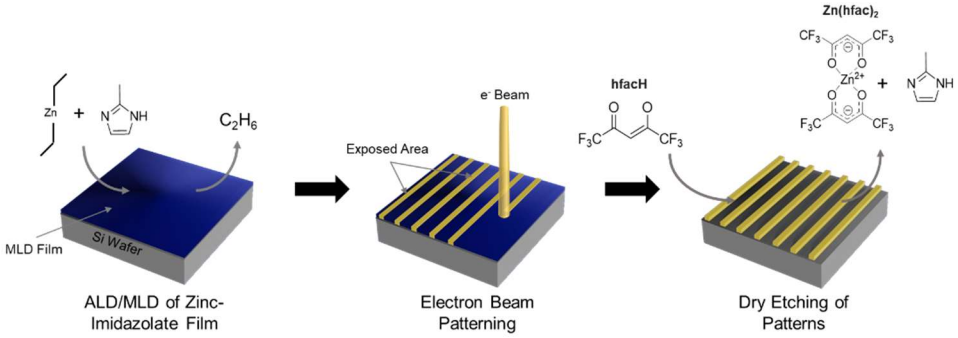

Figure 1. Overall process schematic of film deposition, patterning, and dry etching to create an all-vapor phase resist technology.

Results and Discussion

The overall process of film deposition, e-beam exposure, and dry etching to create an all-vapor phase resist technology is described in **Figure 1**. aZnMIm films are first deposited in a home-built ALD/MLD system using DEZ and 2MIm precursors at 150 ºC before irradiation with an e-beam and subsequent development with hfacH at 120 ºC.

ALD/MLD of Zinc-Imidazolate Thin Films

Crystalline ZIF-8 films have been grown from the vapor phase previously through the reaction of ALD ZnO films with 2-methylimidazole (2MIm) vapors [6], and by CVD from 2MIm and zinc(II) acetylacetonate vapors in the presence of water vapor [33]. Recently, crystalline ZIF-8 films have been grown directly in an MLD process by using water vapor pulses before and after each DEZ pulse and employing 2MIm exposures of at least 400 s [7]. It is important to note that this recent work by Smets et al. aimed to optimize deposition of crystalline ZIF-8 films, while the amorphous deposits they made (in the absence of water vapor pulses) were not smooth, exhibiting roughness on the order of tens of nanometers. Smets et al. further showed that discontinuous amorphous films were formed when using 2MIm exposures of less than 400 s. In contrast, the objective of the current study was to form smooth, amorphous films due to their aforementioned advantages for patterning. To the best of our knowledge, this has only been accomplished from the liquid phase using dilute solutions [30].

The proposed composition of the layer-by-layer deposition is shown in **Scheme 1** and **Figure 2a**. Following the 2MIm pulse, it is expected that half of the 2MIm molecules on the surface of the film would be protonated, a configuration that has been suggested by simulations of ZIF surfaces [38]. In the ALD/MLD process, the remaining protons on the surface 2MIm groups will be transferred to Zn-bound ethyl ligands in the subsequent DEZ pulse to produce a monoethylzinc (MEZ) group bound to two deprotonated 2MIm groups and a molecule of ethane gas. As has been observed in XPS of ZIF films [39] and simulations of ZIF surfaces [38, 40], exposure to humid air may result in the presence of hydroxyl groups due to a ligand exchange between H_2O and 2MIm or remaining MEZ groups. These studies have also found that hydrogenocarbonate groups may be formed from the reaction between hydroxyl groups and carbon dioxide.

Scheme 1: Atomic/molecular layer deposition of ZnMIm

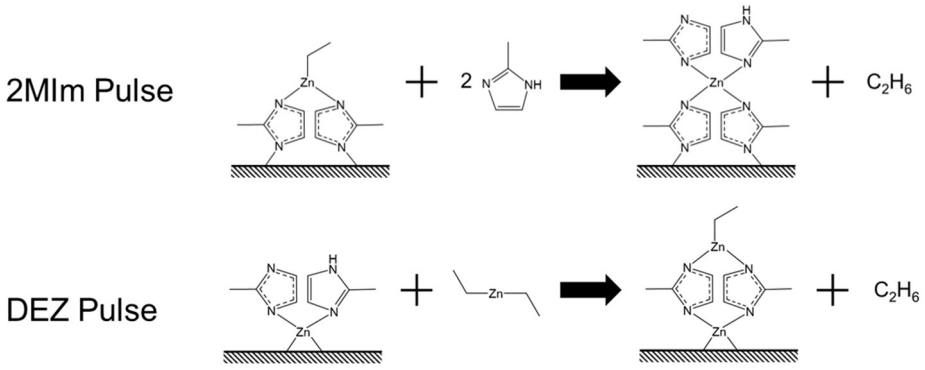

aZnMIm films were deposited on Si wafers using a sequence of **(1)** 50 ms DEZ pulse, **(2)** 30 s Ar purge, **(3)** 100 ms 2MIm pulse, **(4)** 45 s Ar purge at reactor temperatures of 100 to 175 °C as shown in the schematic in Figure 2a. Ex situ ellipsometry of the deposited aZnMIm films in Figure 2b demonstrates that their

thickness is proportional to the number of ALD/MLD cycles, as is expected for ALD/MLD processes and has been observed in many previous studies [5].

No film growth was observed at the lowest tested deposition temperature of 100 °C. It should be noted that the 2MIm cylinder is housed in the reactor oven (Figure S1), so the vapor pressure, and therefore the partial pressure, of 2MIm in the reactor is not independent of the reactor temperature. The lack of observed film growth at 100 °C may thus be attributed to both a reduced reaction rate and a low partial pressure of 2MIm. The growth rate increased from 0.05 nm cycle^{-1} at 125 °C to a maximum of 0.15 nm cycle^{-1} at 150 °C before decreasing slightly to 0.13 nm cycle^{-1} at 175 °C. The plateau in growth rates observed at 150 and 175 °C may be indicative of an ALD window, a temperature range where growth does not directly depend on temperature. Most reported ALD/MLD processes have utilized carboxylic acids or polyols of a wide variety of sizes as the organic component, and there are no comparable studies using only 2MIm and DEZ. Therefore, there is limited literature available with which we could directly compare growth rates [5]. A more relevant ALD/MLD study [41], which also relied on a reaction between a strongly nucleophilic metal-alkyl compound and a protic nitrogen species, observed growth rates of 0.09 to 0.17 nm cycle^{-1} over a temperature range of 200-400 °C for films grown from trimethylaluminum and *p*-phenylenediamine. For both DEZ and 2MIm, reducing the argon purge to less than 15 s resulted in a sharp increase in the growth rate due to CVD-type growth caused by insufficient precursor purging (Figure S2b).

XRD patterns of the aZnMIm films shown in Figure 2c demonstrate that the aZnMIm films are amorphous at all deposition temperatures examined. Atomic force microscopy (AFM) (Figure S3) of the films confirm that they are continuous and smooth, with a root mean square (RMS) surface roughness of 0.195 nm. In addition, excellent spatial uniformity of the deposited films was demonstrated by deposition on 200 mm diameter Si (111) wafers, with a film thickness variation 6% or less from the average value for all regions of the wafer as measured by ex situ ellipsometry (Figure S4).

Although the focus of this manuscript is on aZnMIm films and their use in e-beam patterning, we also report on their transformation to crystalline ZIF-8 using 2MIm vapor treatment in a separate batch reactor in section S1 and Figures S5 to S7. We use these crystalline ZIF-8 films, which we name *aZnMIm-ZIF-8,* along with ZIF-8 films made by treating ALD ZnO films with 2MIm vapors [6], which we call here *ZnO-ZIF-8*, to compare their morphology and vibrational spectra with those of aZnMIm films.

IRRAS spectra of the aZnMIm films grown on an Au-coated Si wafer demonstrate that they are chemically similar, but not identical, to crystalline *ZnO-ZIF-8* (Figure 2d) and *aZnMIm-ZIF-8* films (Figure S2c). Peaks at 3130 and 2925 cm^{-1} attributed to aromatic =C–H and methyl C–H stretching, respectively, are present, but are broadened and diminished compared to those of *ZnO-ZIF-8* and *aZnMIm-ZIF-8* [42]. The broad peak in the region of 1585 cm^{-1} is attributed to C=N stretching [43] or N-H bending from moieties with missing Zn defects (M. Ahmad, work in preparation) and peaks at 1460 and 1420 cm^{-1} correspond to methyl C–H bending. Interestingly, peaks at 1305 (C–H_{ring} in-plane rocking), 1170 (C–H_{ring} in-plane deformation), 1140 (=C–H in-plane deformation), and 995 (methyl C–H bending and in-plane C–H_{ring} rocking) cm^{-1} are broadened and shifted 5-10 cm^{-1} lower than the corresponding peaks in *ZnO-ZIF-8*, suggesting that the chemical environment is less uniform than crystalline ZIF-8, as expected for an amorphous material.

The aZnMIm films were also characterized by XPS, as shown in Figure 2e and Figure S8, which revealed spectra that are almost identical to those of crystalline ZIF-8 [28]. Specifically, the C:N:Zn ratio is found to be 20.6:5.3:1. The presence of oxygen is consistent with previous studies where ZIF films were grown by vapor phase conversion of ALD ZnO films [44-45]. As previously discussed, this oxygen is attributed to

surface hydroxyl groups or carbonates formed after exposure to humid air, as has been observed in XPS of ZIF films [39] and simulations of ZIF surfaces [38, 40]. A brief Ar^+ sputter was applied to remove most of the surface oxygen and adventitious carbon. Indeed, after Ar^+ sputtering, the C:N:Zn ratio was 9.4:3.4:1, which is very close to the predicted ZIF-8 C:N:Zn ratio of 8:4:1.

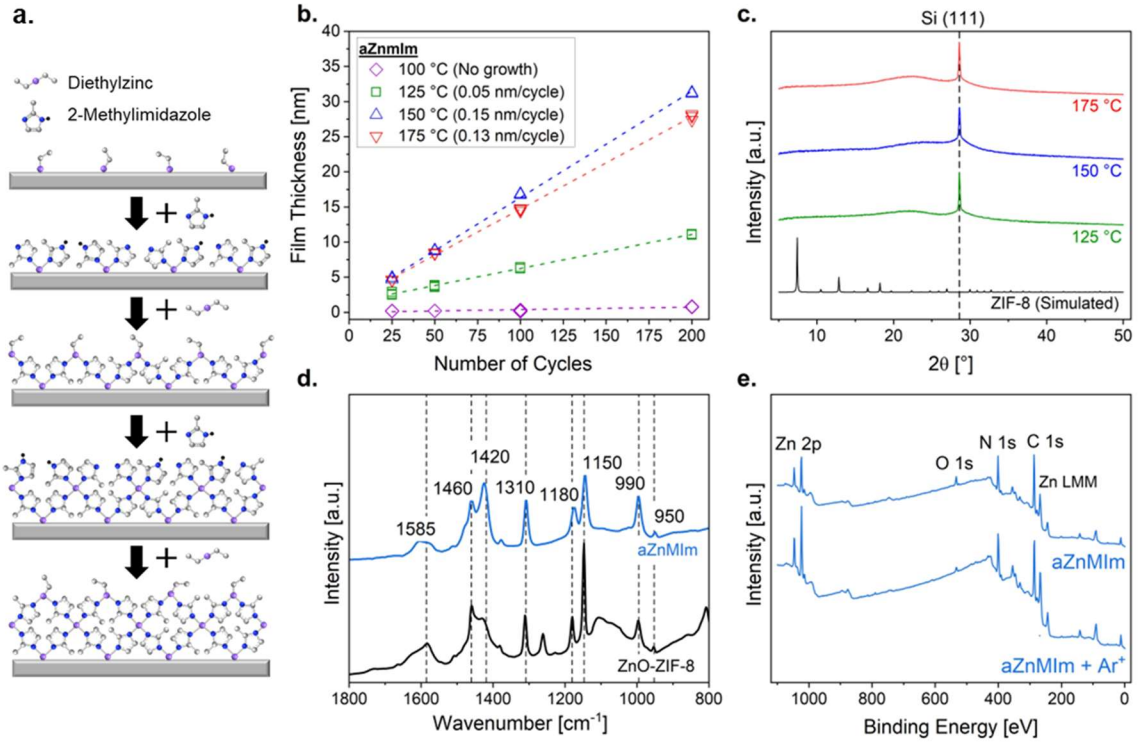

Figure 2. ALD/MLD Film Growth and Characterization. (a) Proposed layer-by-layer growth mechanism. (b) Deposited aZnMIm film thickness as measured by ex situ ellipsometry as a function of the number of MLD cycles. (c) XRD patterns of aZnMIm films deposited at the indicated temperatures. (d) IRRAS spectra from 1800-800 cm^{-1} of (top) an aZnMIm film and (bottom) a *ZnO-ZIF-8* film. (e) XPS survey scans from 1100-0 eV of (top) an aZnMIm film and (bottom) an aZnMIm film following 10s of Ar^+ sputtering to remove the surface layer. The aZnMIm films were deposited at 150 °C in 400 cycles with a final thickness of 60 nm using a deposition sequence of (1) 50 ms DEZ pulse, (2) 30 s Ar purge, (3) 100 ms 2MIm pulse, (4) 45 s Ar purge. The *ZnO-ZIF-8* films were prepared by a two-hour reaction of a 14 nm thick ZnO film deposited in 100 cycles of ALD using DEZ and H_2O, with 2MIm vapors in a batch system at 120 °C at a base pressure of 5 x 10^{-2} mbar to produce films with a final thickness of 100 nm.

We emphasize that the ALD/MLD reaction conditions used herein resulted in smooth (RMS roughness of 0.195 nm) and continuous amorphous films with Zn:N ratio and vibrational spectra nearly identical to those of crystalline ZIF-8, in contrast to the films obtained by Smets et al. in which depositions using only DEZ and 2MIm resulted in rough amorphous films [7]. This difference may be attributed to the lower substrate temperature of 80 °C and 2MIm evaporation temperature of 125 °C used in this previous study, compared to those used in our experiments.

Etching of aZnMIm Films by hfacH

Having shown that smooth, amorphous ZnMIm films can be produced by ALD/MLD, a patterning and etching process was developed to realize the process outlined in Figure 1. Specifically, potential volatile

etchants capable of selectively removing as-deposited aZnMIm while leaving e-beam irradiated areas unaffected were investigated. The β-diketone etchant hfacH was found to etch aZnMIm films (**Figure 3a**), while e-beam irradiated aZnMIm was etch resistant. The ability of hfacH to etch aZnMIm films allowed for facile vapor phase development of features patterned in aZnMIm films by EBL.

Figure 3b shows XPS data describing the effect of hfacH on 20 nm thick aZnMIm films at an etching temperature of 120 ºC. In the as-deposited aZnMIm films (aZnMIm), Zn, C, O and N are detected, while aZnMIm films exposed to hfacH for 30 minutes (aZnMIm + hfacH) have an XPS spectrum almost identical to that of a silicon wafer, indicating that these reaction conditions are sufficient to completely etch the aZnMIm film. Etch rate determination was attempted by decreasing the duration of hfacH exposure. XPS data (Figure S9) revealed that exposure times as short as 60 seconds were sufficient to etch all but trace quantities of the 60 nm aZnMIm films. These data suggest that the etch rate of aZnMIm with hfacH is greater than 60 nm min^{-1}, although the potential for a small amount of hfacH to remain in the reactor during the subsequent Ar purge step may also contribute to etching, so the actual etch rate may be slightly lower. Following etching at these short exposures, a small amount of Zn remains that shows increased etch resistance and may be attributed to Zn at the Si – aZnMIm interface. Data for 4 nm ZnO films etched under identical conditions (Figure S10) show almost no etching after a 60 second hfacH exposure, and only a decrease in film thickness of approximately 1 nm after 30 minutes of etching, corresponding to an etch rate of 0.03 nm min^{-1}. The etch rate for aZnMIm with hfacH is therefore several orders of magnitude faster than ZnO with hfacH. Etching of ZnO has been shown by Droes et al. to occur in a temperature range of 130 to 500 ºC under a 27 mbar partial pressure of hfacH. At a temperature of 350 ºC, a maximum etch rate of 317 nm min^{-1} was observed, whereas at higher temperatures, decomposition of reactants or products resulted in C and F contamination. At their minimum tested etching temperature of 130 ºC, the etch rate is significantly reduced to 0.6 nm min^{-1} [17]. Our etch rate is lower than that shown by Droes et al. for ZnO etching with hfacH likely due to the lower temperature (120 ºC) and pressure (6.5 mbar) of hfacH used in this study. The low temperature required for etching the as-deposited aZnMIm films is particularly relevant for integration into a lithographic process, as it falls within the range typically used for pre-exposure and post-exposure baking of polymer photoresists like ZEP520A [46]. This temperature is also significantly lower than those used for other dry etching processes, e.g., etching of ZrO_2 and Al_2O_3, which are typically in excess of 250 ºC [47].

Based on etching reactions of hfacH with NiO proposed by Basher [48] and ZnO proposed by Kung and Teplyakov [49], a reaction scheme for hfacH etching of aZnMIm is proposed in **Scheme 2** and expressed in Figure 3a. In the etching of metal oxides, adsorption of hfacH with a proton transfer to oxygen in the metal oxide is followed by desorption of a metal hfac complex and water. While no example of hfacH etching of inorganic-organic hybrid thin films has been shown in the literature, this novel process is postulated to include a proton transfer from hfacH to a 2MIm anion to form a volatile 2MIm molecule along with binding of the deprotonated hfac to Zn^{2+}. After the coordination of two hfac molecules to Zn^{2+} ions, volatile $Zn(hfac)_2$ and two 2MIm molecules can desorb from the surface. The volatility of both $Zn(hfac)_2$ and 2MIm molecules at 120 ºC are key factors that contribute to facile etching at such low temperatures.

Scheme 2. Etching of aZnMIm films using hfacH

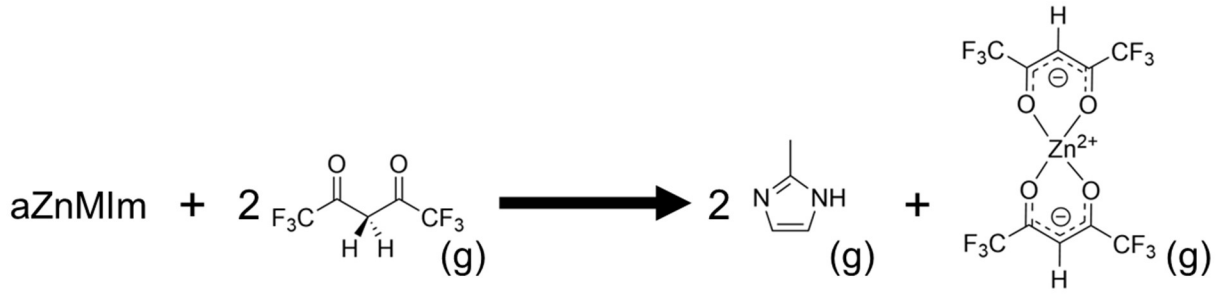

Electron Irradiation of aZnMIm Films

We now proceed to demonstrate that e-beam exposure alters the chemical structure of aZnMIm films as probed by vibrational spectroscopy, while XPS shows Zn:N ratios before and after irradiation are unchanged. XPS analysis of electron irradiated aZnMIm films (aZnMIm + e^-) in Figure 3c shows no significant change in the C:N:Zn ratio of the film, except for the addition of a small amount of e-beam-deposited carbon which can be removed by a brief Ar^+ sputter to recover a film whose C:N:Zn ratio is similar to that of the as-deposited aZnMIm film (Figure S11). A more detailed analysis of the XPS peaks (Figure S8) reveals peak broadening and a loss of the π-π* shake up peak in the C (1s) region associated with the imidazolate ring [50] after irradiation, indicative of electron induced degradation of 2MIm.

In marked contrast to the effect of hfacH exposure on as-deposited aZnMIm films (aZnMIm + hfacH), XPS data shows relatively little change for electron-irradiated aZnMIm films after hfacH exposure (aZnMIm + e^- + hfacH), except for some Zn depletion and the appearance of a small amount of F on the film surface. Surface Zn depletion seen in aZnMIm films following hfacH exposure and electron irradiation (aZnMIm + e^- + hfacH) is likely caused by hfacH removal of exposed surface Zn atoms that are still present after e-beam irradiation; however, hfacH is unable to diffuse beneath the irradiated aZnMIm surface because the imidazole linkers have been degraded and the aZnMIm film has been converted to a more dense, non-volatile matrix after e-beam irradiation. In contrast, Zn removal occurs more readily for as-deposited aZnMIm (aZnMIm) because volatile 2MIm is continually removed, allowing for deeper lying Zn atoms to be accessed. The appearance of surface fluorine is likely a result of C–CF_3 and C–F bond cleavage caused by hfac decomposition, analogous to previous XPS studies of ZnO surfaces after exposure to hfacH [49]. As was seen prior to hfacH exposure, a brief Ar^+ sputter is sufficient to recover a film (aZnMIm + e^- + hfacH + Ar^+) whose composition is comparable to the aZnMIm film, confirming that F and O are limited to the film surface while the bulk of the irradiated film remains unchanged. Thus, in contrast to the aZnMIm films, the e-beam modified film is resistant to etching by hfacH.

Scanning electron microscopy/energy dispersive spectroscopy (SEM-EDS) data acquired on 20 nm thick aZnMIm films before and after electron irradiation reveal film elemental ratios of Zn, C, N, and O unaffected by electron irradiation, a finding consistent with the low contrast between irradiated (aZnMIm + e^-) and non-irradiated areas (aZnMIm) (Figure S12) as well as the inference from the XPS data. Following exposure to hfacH, however, there is visible contrast in the SEM images between the irradiated (aZnMIm + e^- + hfacH) and non-irradiated areas (aZnMIm + hfacH) (Figure 3e). Furthermore, in irradiated areas (aZnMIm + e^- + hfacH), the C, N, and Zn peaks detected in the aZnMIm film remain while in non-irradiated areas (aZnMIm + hfacH), a complete loss of the Zn and N peaks is observed leaving only the Si, O, and C peaks expected for a silicon wafer (Figure 3f). Despite the invariant C:N:Zn ratio within the aZnMIm film

upon irradiation (aZnMIm + e^-), the electron induced degradation of 2MIm is evidenced in the IRRAS data shown in Figure 3d by the complete loss of the 2MIm vibrational modes detected in the as-deposited aZnMIm films. This is ascribed to electron induced dehydrogenation by C–H and N–H bond cleavage, which has been previously observed in amines exposed to electron irradiation [51] and ring opening shown by Meissner et al. for electron ionization of imidazole [52], providing a rationale for the loss of conjugation evidenced in XPS by the disappearance of the π-π* feature.

As a consequence of electron irradiation, porous ZIFs have exhibited densification and pore volume contraction owing to local structural changes [29, 53-54]. In this study, AFM from a partially irradiated aZnMIm film (Figure S13) demonstrates a dose-dependent height depression with an approximate 5% height depression in areas irradiated with a dose of 10 mC cm^{-2} (e.g., decrease of 3.3 nm from an initial thickness of 60 nm), while the height of the non-irradiated area remains constant. Under the same irradiation conditions, Miao and Tsapatsis [29] noted a ca. 10% height decrease of the e-beam exposed areas on a 290 nm thick ZIF-L single crystal. Differences in the degree of film contraction between aZnMIm and ZIF-L are likely a consequence of the higher density of aZnMIm films compared to conventional porous ZIF materials. In support of this idea, Widmer et al. found that dense ZIF-zni experienced a significantly smaller irradiation-induced volume contraction of only 2% compared to nearly 20 and 15% for porous ZIF-4 and ZIF-62, respectively [53].

Collectively, the XPS, SEM-EDS, IRRAS, and AFM data of irradiated films point to electron induced densification and transformation of aZnMIm into an amorphous carbon nitrogen film containing Zn that is resistant to hfacH etching at 120 °C. As shown in Scheme 2, the as-deposited films can react with hfacH to form volatile $Zn(hfac)_2$ and 2MIm species when Zn^{2+} is removed by hfacH during etching of unmodified aZnMIm allowing for continued removal of the film. In contrast, there is no pathway for the formation of volatile carbon and nitrogen species once the 2MIm linkers have been degraded by electron irradiation and consequently only Zn^{2+} exposed at the surface can be etched by hfacH with the remaining elements of the film remaining.

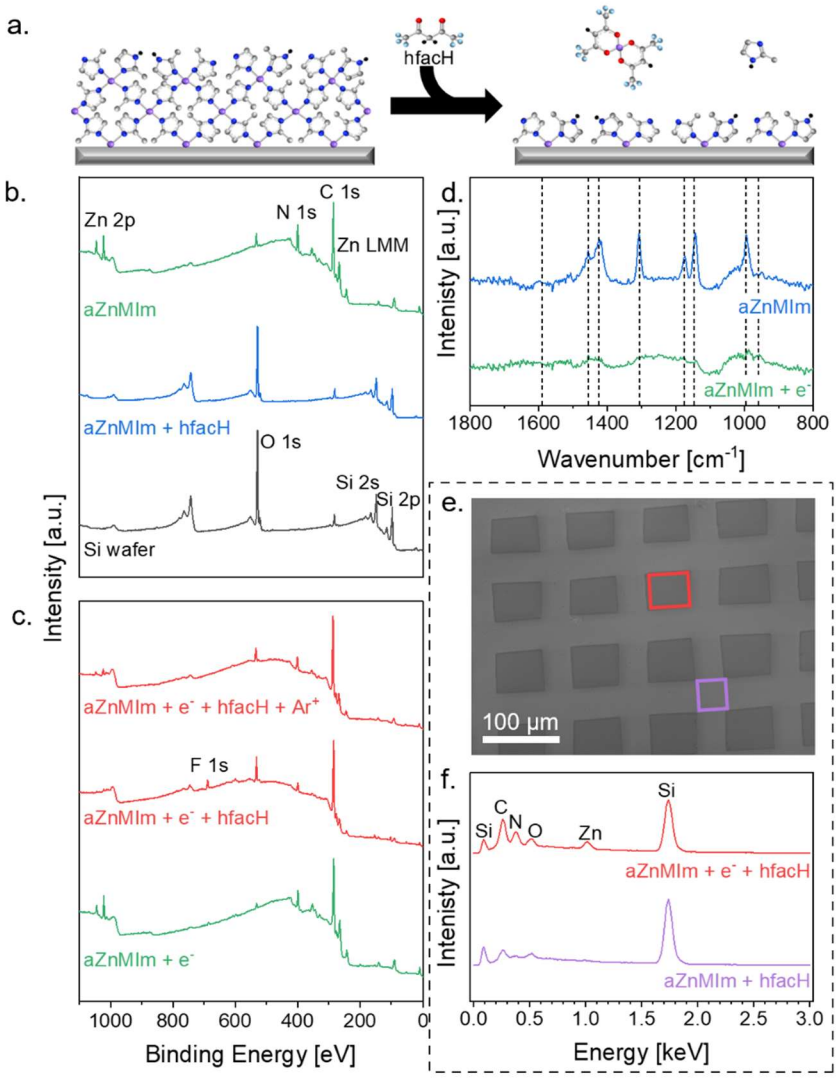

Figure 3. Effect of hfacH on as-deposited and electron irradiated amorphous zinc-imidazolate (aZnMIm) films. (a) Etching of aZnMIm films using hfacH (Carbon in gray, fluorine in light blue, hydrogen in black, nitrogen in dark blue, oxygen in red, zinc in purple) (b) XPS spectrum of an aZnMIm film before and after hfacH exposure, showing complete etching of the aZnMIm. (c) XPS spectrum of electron beam irradiated aZnMIm films before hfacH exposure, after hfacH exposure, and after hfacH exposure followed by a brief Ar^+ sputter. (d) IRRAS spectrum of as-deposited and electron irradiated aZnMIm films. Electron irradiation was achieved using a UHV chamber with an e-beam operating at a voltage of 2 kV, an electron flux of 1.3 µA cm^{-2}, and a calculated dose of approximately 4 mC cm^{-2}. (e) SEM image of large-scale masked pattern made with a 2 keV electron beam. (f) EDS spectrum of irradiated and non-irradiated areas within the SEM image. All etched samples were exposed to hfacH for 30 minutes at 120 °C under a flow of argon.

Direct-Write Electron Beam Lithography on aZnMIm Films

Based on the selective hfacH etching of as deposited films as compared to electron irradiated films, we explored the lithographic properties of aZnMIm films. Due to the limited availability of EUVL systems, EBL is often used as a surrogate for EUVL as both irradiation sources cause the emission of low energy

secondary electrons that are responsible for the chemical transformations in resists. In addition, it has been demonstrated that EBL can be used as a probe to predict EUV sensitivity [55].

aZnMIm films deposited on silicon wafers were exposed to electrons using energies between 5 and 30 keV at various doses and subsequently developed with hfacH at 120 °C to generate the dose matrix patterns shown in the AFM images in **Figures 4a** and S14. These data were then used to generate the resist contrast curves in Figure 4b. The measured thickness of each square in the dose matrix was zero for electron doses below thresholds of approximately 3, 6, and 8 mC cm^{-2} for 5, 20 and 30 keV, respectively. As expected from the XPS, SEM, and IRRAS results described in Figure 3, Figure 4a demonstrates that aZnMIm functions as a negative tone resist following hfacH exposure.

Resist sensitivity, defined as the dose required to retain 50% of the normalized thickness, is a critical performance benchmark because more sensitive resists allow for shorter exposure times and higher throughput. The aZnMIm resist sensitivities calculated from Figure 4b are 5.5, 28, and 37 mC cm^{-2} for acceleration voltages of 5, 20, and 30 kV, respectively. The increase in required dose at higher acceleration voltages, as depicted in Figure 4b, is typical of e-beam resists. This phenomenon arises because the probability of an electron interaction event within the resist decreases with higher incident electron energy, so more primary electrons are required to increase the frequency of electron interaction [56]. In context, the sensitivity values for aZnMIm are high compared to conventional resists (common negative tone e-beam resist HSQ has a sensitivity of 2.5 mC cm^{-2} at 100 keV using a salty developer [57]) but are within the range of other negative tone metal-containing resists such as metal sulfide-based zinc butylxanthate resists which have a sensitivity of 46 mC cm^{-2} at 100 keV [58], metal carboxylate-based zinc naphthenate resists which have a sensitivity of 15 mC cm^{-2} at 100 keV [59], and PFpP-based metal-carbonyl organometallic polymer resists which have a sensitivity of 12 mC cm^{-2} at 20 keV [60]. It is important to note that the resists included in the aforementioned works were developed in solution and no literature on e-beam sensitivity of other all-dry negative tone metal-containing resists exists for appropriate comparison. The Zn and/or 2MIm ligands could however be substituted for more sensitive groups or those with double bonds more suitable for crosslinking in an effort to improve the negative tone aZnMIm resist sensitivity.

Lithographic contrast (γ) is another important resist property, reflecting its ability to differentiate between the properties of irradiated and non-irradiated areas. Contrast is important when considering resolution limitations in densely patterned areas where proximity effect will cause areas next to patterns to receive a non-zero dose. The contrast can be calculated using $\gamma = \frac{1}{\log(D_{100}/D_0)}$, where D_{100} is the lowest electron dose at which the original resist thickness is retained and D_0 is the maximum electron dose for which the resist thickness equals zero. γ, which is expected to vary slightly at different accelerating voltages due to changing beam broadening and electron interaction volume [61], was calculated from the values in Figure 4b as 1.35, 1.0, and 0.87 at 5, 20, and 30 keV, respectively. These values are comparable to other negative tone metal-containing resists such as ALD/MLD Hf-based hybrid thin films (γ = 1.7) [13], MOF inspired Zn-cluster containing films (γ = 2.3) [20], and various organotin polymeric hybrid resists (γ = 1.55 – 2.54) [62]. γ is a function of processing conditions such as the development method, use of pre or post exposure baking, and the lithography tool used for patterning, so further process optimization may increase the observed contrast. It should be noted that the etching conditions used herein for pattern generation are far in excess of what the etching studies have indicated is required for complete removal of the as-deposited aZnMIm film (less than 60 s for a 60 nm thick film). Longer etching times consistently produced high resolution patterns for densely spaced features but resulted in lower contrast and sensitivity.

AFM characterization of Figures 4c-f demonstrates a variety of well-resolved patterns on silicon wafers prepared by exposing aZnMIm films to electrons at 30 keV and 200 mC cm^{-2} followed by development with hfacH for 30 minutes (6 cycles) at 120 ºC. Dot patterns (Figure 4c) were used to probe the smallest achievable spot size, which was found to be 25 nm in diameter. Isolated line patterns in Figure 4d demonstrate lines 29 nm wide that experience approximately 10 nm of broadening due to proximity effect scattering as the nominal line thickness was 20 nm. The AFM height profile (Figure 4e) of the trace in Figure 4d shows that there is complete removal of the non-irradiated aZnMIm film between the lined features. Multiple line widths and spacings were tested in the example pattern shown in Figure S16 to ascertain the resist critical feature dimensions. As shown in the AFM image in Figure 4f, the 29 nm lines (20 nm nominal) are well-resolved until a pitch of 40 nm, after which the lines become blurred together. Variations from the desired pattern are attributed to reduced electron beam uniformity resulting from charging of the insulating aZnMIm film and/or beam drift during patterning resulting from a large dwell time and slow beam speed required to pattern at the desired dose. Line roughness measurements were taken from the high-resolution inset in Figure 4f, giving a line edge roughness (LER) of 3.47 nm, and a corresponding line width roughness (LWR) of 4.77 nm for the 50 nm pitch lines (Figure S15).

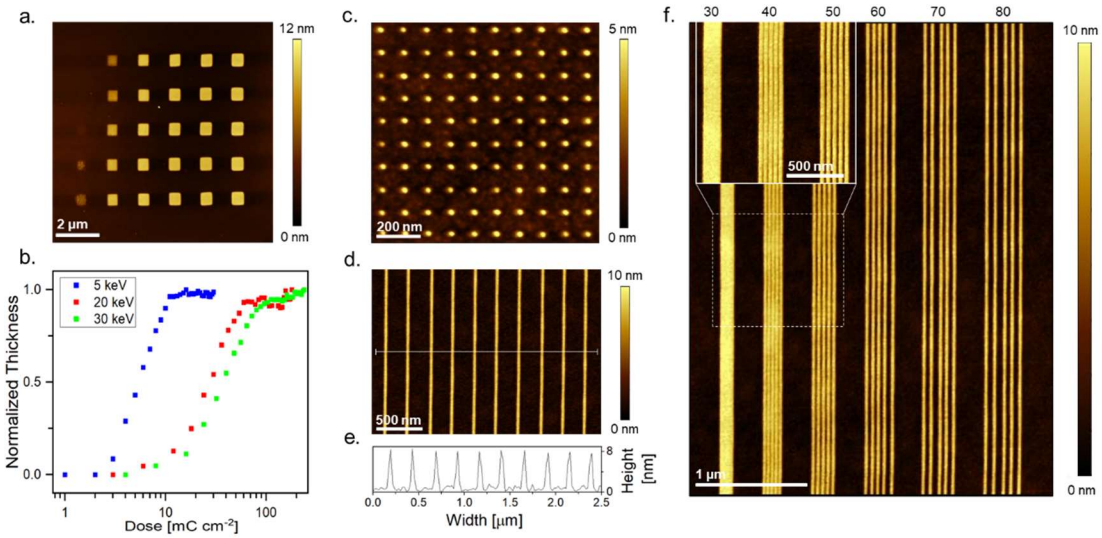

Figure 4. aZnMIm patterning on silicon wafer substrates. (a) AFM image of a dose matrix pattern used to construct the contrast curve in (b). Squares are 500 nm by 500 nm with a pitch of 1.5 µm and were patterned at 5 keV with a base dose of 1000 µC cm^{-2}. The top left corner starts with a dose factor of 1.0. The dose factor of each subsequent square increases by 1.0 until the bottom right square has a dose factor of 30. (b) Contrast curves for an aZnMIm resist deposited on a Si wafer and patterned at 5, 20, and 30 keV. Normalized thicknesses were determined using AFM height profiles. (c) AFM image of a 100 nm pitch dot pattern with dots 25 nm in diameter. (d) AFM image of a pattern with 29 nm wide and 250 nm pitch lines. (e) Height profile following the line marked by the trace in (d). (f) AFM image of a line spacing gradient pattern with numbers representing the line pitch. All line widths in (f) are approximately 29 nm. Irradiated samples were exposed in a Raith e-line. All etched samples were exposed to hfacH for 30 minutes at 120 ºC under an imposed argon flow. All films had a thickness of ca. 10 nm as determined by ellipsometry.

To pattern under conditions with minimal secondary and backscattered electrons from the Si substrate, aZnMIm films were deposited and patterned on 15 nm thick silicon nitride (SiNx) TEM substrates, shown schematically in **Figure 5a**. Patterns on SiNx were characterized by TEM due to the substrate being too

flexible for AFM measurements. Figures 5b and 5c demonstrate well resolved aZnMIm line patterns on SiNx prepared by EBL and followed with development by hfacH etching for 30 minutes (6 cycles) at 120 °C. The isolated line pattern in Figure 5b shows 25 nm lines patterned at 20 keV, 0.1 nA, and 80 mC cm^{-2}. Multiple line widths and spacings were also tested on SiNx from the example pattern shown in Figure S16 to ascertain the resist critical feature dimensions. The TEM image in Figure 5c demonstrates well resolved 22 nm lines with a pitch of 30 nm patterned using an electron energy of 30 keV, a current of 0.1 nA, and a calculated dose of 40 mC cm^{-2}. The TEM image in Figure S17 shows that for 10 nm nominal lines that experience broadening of about 15 nm, the smallest resolvable pitch is 30 nm, after which the lines become blurred. The resolution limits of the aZnMIm resist have likely been reached under the current processing conditions, however, patterning at higher beam energies as well as further optimization of development conditions (etchant, time, and temperature) may decrease critical feature dimensions.

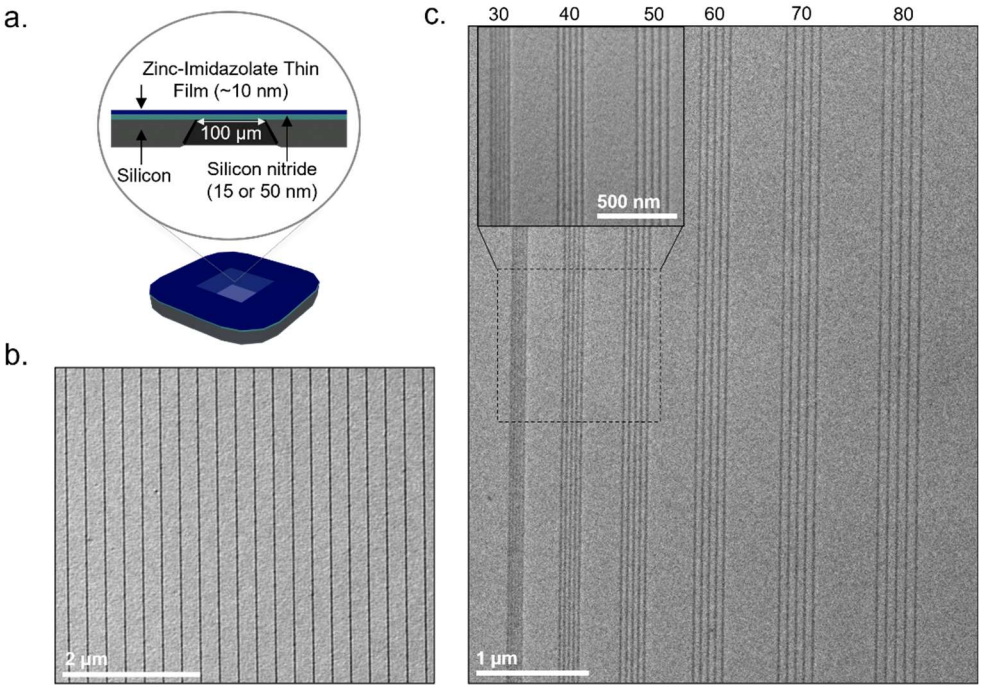

Figure 5. aZnMIm patterning on thin silicon nitride (SiNx) support. (a) Schematic illustration of a SiNx TEM support. (b) TEM image of a pattern with 25 nm wide and 250 nm pitch lines patterned at 20 keV with a dose of 80 mC cm^{-2}. (c) TEM image of a line spacing gradient patterned at 30 keV and a dose of 40 mC cm^{-2} with numbers representing the line pitch. All line widths are approximately 22 nm. Film deposition for the patterns in (b) and (c) was conducted on a 15 nm thick SiNx TEM support. Irradiated samples were exposed in a Helios G4 FIB SEM with a current of 100 pA and a dwell time of 1 µs. All etched samples were exposed to hfacH for 30 minutes at 120 °C under an imposed argon flow. All films had a thickness of ca. 10 nm.

Scanning transmission electron microscopy/energy dispersive spectroscopy (STEM-EDS) was conducted on a patterned aZnMIm film deposited on a 15 nm thick SiNx TEM support (Figure S18) to determine if complete removal of aZnMIm in non-irradiated areas is observed on the nanometer scale between lined features after hfacH etching. STEM-EDS mapping reveals that the material left behind after irradiation and etching is rich in Zn, C, and N with an even distribution of each element throughout the patterned features. Analysis of the non-irradiated areas demonstrated a near complete depletion of the Zn peak associated with aZnMIm, while the N and Si peaks associated with the SiNx substrate increased. Fluorine was not detected

in either area. These findings are consistent with the micrometer scale SEM-EDS data acquired in Figure 3e-f, further supporting the idea that non-irradiated aZnMIm can be completely etched by hfacH, while electron irradiated aZnMIm regions are more resistant to hfacH etching.

The successful use of EBL for these films suggests that they would be a promising candidate for EUV lithography. Over 250 ZIFs have been synthesized to date, with documented ZIF structures using dozens of different imidazole linkers and over 15 different metals [23, 63]. By using the proper selections of linkers and metalorganic precursors, it should be possible to develop other dry-deposited metal-imidazolate resists with improved sensitivity, contrast, and critical dimensions by incorporating elements with higher EUV absorption cross sections such as indium and iodine. Optimization of the electron dose and acceleration voltage, etchant selection, and etching conditions may lead to further improvements in the resist properties as well. For example, increasing the beam operating voltage to 100 kV is expected to reduce feature blurring resulting from proximity effect and decrease the minimum feature size allowing for smaller pitch sizes to be resolved. Preliminary results showing a dose matrix pattern and its corresponding contrast curve prepared using a 100 keV electron source are shown in Figure S19.

Previous all-dry processes have typically focused on the use of dry deposition methods like plasma polymerization and chemical vapor deposition (CVD) followed by dry development with plasma etchants [64] or high-pressure supercritical CO_2 [65]. Physical vapor deposition of molecular glasses followed by polymerization-inducing UV patterning and vacuum development to evaporate only the non-exposed areas that were not polymerized has also been reported [66]. Recently, LAM Research announced an all-dry EUV photoresist system through a collection of patents and a conference presentation. In their patent titled "Dry Development of Resists", LAM Research proposes dry development of EUV-sensitive organo-metal oxide or organo-metal-containing resists deposited via both vapor phase and spin-coating methodology through the use of either a gentle plasma or a thermal process using a flowing Lewis acid vapor like BCl_3 [4]. Further work in "Positive Tone Development of CVD EUV Resist Films" describes a method for dry deposition of photoresists (tin-based in some embodiments) and their subsequent wet development with the option of an additional thermal (HCl or HBr halide), plasma, or a combined thermal and plasma dry development gas to be applied for further processing after wet development to improve tunability, critical dimension control, and scum control [19]. Experimental data and line patterns describing results with a dry deposited photoresist and a positive tone solution phase TMAH developer is included. In their most recent patent application "Photoresist Development with an Organic Vapor", LAM Research claimed dry development of wet or dry deposited metal-containing resists using organic vapors such as carboxylic acid, trifluoroacetic acid, and hfacH, but no experimental demonstration of their use as dry etchants is included [18]. In a presentation from LAM Research, an all-vapor phase process was reported that employs vapor deposition of small metal-organic units to form a photoresist that has achieved resolution as low as 12.9 nm with a pitch of 26 nm after EUV exposure and solvent-free etching, although their processing details and method of dry development have not been reported [3]. Compared to traditional wet deposited and developed resists, LAM's all-vapor phase technology has demonstrated a reduction in defects that can lead to electrical failures in devices as well as improvements in feature blurring and the formation of complex high aspect ratio pillars, highlighting the industrial desirability of all-vapor phase methods. Moreover, all-dry resist processing methods can be used on non-conventional curved surfaces, eliminate the requirement for stabilization agents or adhesion promoters that are often required for spin coated resists, circumvent pattern collapse due to capillary forces during wet development, and reduce processing cost and waste production by 5-10x due to the elimination of significant solvent waste generation during both deposition and development [3-4, 28, 67].

Conclusion

A novel all-dry resist technology was demonstrated using direct molecular layer deposition of an amorphous zinc-imidazolate (aZnMIm) thin film and subsequent dry development of e-beam-patterned films using hfacH, a model β-diketone-type compound. This process has been made possible by the new application of a low temperature (120 ºC) etching method using hfacH that can selectively remove as-deposited aZnMIm while retaining e-beam irradiated aZnMIm. This methodology produces a solvent free, EUV compatible process that allows for cost-effective and high-resolution resist development with critical dimensions down to 22 nm lines with 30 nm pitch on SiNx substrates and 29 nm lines with 40 nm pitch on Si wafer substrates. Further work will focus on the optimization of both etching conditions and the combination of linker and metal organic precursor in order to increase resist contrast and sensitivity, in addition to the investigation of etch resistance and pattern transfer. Patterning by EUVL and higher voltage (100 kV) state of the art EBL systems will also be explored.

Experimental

Materials: Diethylzinc (DEZ) (95%, Strem Chemicals), 2-methylimidazole (2MIm) (99%, Millipore-Sigma), and argon (Ar) gas (>99.999%, AirGas) were used as received without further purification. 1,1,1,5,5,5-hexafluoroacetylacetone (hfacH) (98%, Sigma Aldrich) was purified with three freeze-pump-thaw cycles before use. Homemade Milli-Q DI water (H_2O) was used. Silicon (111) wafers were purchased from UniversityWafer Inc. Silicon nitride (SiNx) TEM supports with nine 100 x 100 μm viewing windows (15 nm thick silicon nitride film on a 200 μm silicon frame) were purchased from Ted Pella. Au-Si substrates for IRRAS were prepared by depositing a 5 nm adhesion layer of Ti and a 100 nm Au layer on Si (100) (UniversityWafer Inc.) substrates using a thermal/e-beam evaporator at a pressure < 1 x 10^{-6} mbar.
X-ray Diffraction (XRD): XRD patterns were collected using a Rigaku MiniFlex powder X-ray diffractometer at 40 kV and 15 mA using a Cu Kα source (λ = 1.5406 Å) in a 2-theta range of 5 to 50º at a step size of 0.02º and a scan rate of 1º min^{-1}.
Ellipsometry: Film thicknesses were measured using a Film Sense FS1 ellipsometer using four LEDs with wavelengths between 465.27 and 641.13 nm. SiO_2 thickness was measured using the built-in SiO_2 on Si model and deposited film thicknesses were measured with a Cauchy model.
X-ray Photoelectron Spectroscopy (XPS): XPS spectra were acquired on a non-monochromatic PHI 5600 XPS using 1253.6 eV Mg Kα X-rays at a power of 300 W. Survey scans were acquired at a pass energy of 178.95 eV. High-resolution scans were acquired at a pass energy of 23.5 eV. For sample sputtering, 1kV Ar^+ ions were used with an ion current of 1.35 μA rastered over a 7x7 mm area.
Atomic Force Microscopy (AFM): All AFM images, except those shown in Figure S13, were collected on a Bruker Multimode 8 operating under standard tapping mode in air with a super sharp silicon reflective aluminum coated (SSS-NCHR) probe at a scan rate of 0.7 Hz and 512 lines/scan. The AFM image in Figure S13 was obtained using a pyrex nitride probe (PNP-TR) with a reflective gold coating on a Bruker Multimode 8 operating under contact mode in air. The images were processed in Gwyddion to align rows and correct horizontal scars. Line-scans were taken by averaging over two adjacent scans. Root mean square surface roughness values were taken as the moment-based RMS roughness (S_q) value found within the Gwyddion Statistical Quantities function.
Infrared Reflection-Absorption Spectroscopy (IRRAS): Infrared reflection absorption spectroscopy (IRRAS) of aZnMIm and *ZnO-ZIF-8* films was performed at Brookhaven National Laboratory using a Bruker Vertex 80V spectrometer and a mercury-cadmium-telluride (MCT) detector cooled to 77 K [36]. The angle was approximately 82° from the surface normal, and spectra were collected by taking an average of 500 scans in the range of 4000-800 cm^{-1} at 4 cm^{-1} resolution at room temperature and under a chamber pressure of < 1 x 10^{-8} torr. A gold film was used as a support to improve the IRRAS signal for these

measurements. These spectra are shown in Figure 2d. Spectra for as-deposited and etched aZnMIm films were acquired on a Shimadzu IR Prestige21 FTIR Spectrometer with a VeeMaxII reflectance accessory at an angle of approximately 80° from the surface normal. Spectra were collected between 4000-400 cm^{-1} at a resolution of 4 cm^{-1}. Spectra were baseline corrected in Spectragryph [37]. These spectra are shown in Figure 3d.

Scanning Electron Microscopy (SEM) and Energy Dispersive X-Ray Spectroscopy (EDS): SEM images were acquired with a Tescan MIRA3 Scanning Electron Microscope at an acceleration voltage of 5 kV. A ThermoFisher Helios G4 UC DualBeam with an EDAX Octane Elite EDS system was used for elemental analysis. An acceleration voltage of 3 kV was used for EDS analysis.

Transmission Electron Microscopy (TEM) and Scanning Transmission Electron Microscopy/Energy Dispersive Spectroscopy (STEM-EDS): TEM image acquisition was performed on both a JEOL F200 Transmission Electron Microscope operating at an acceleration voltage of 200 kV (Johns Hopkins University) and a JEOL JEM-1400Flash Transmission Electron Microscope operating at an acceleration voltage of 120 kV (Morgan State University). The images were processed in Digital Micrograph to correct pattern rotation and to increase image brightness and contrast. STEM-EDS was performed on the JEOL F200 Transmission Electron Microscope operating at an acceleration voltage of 200 kV with a collection time of approximately 5 minutes.

Direct-Write Electron Beam (e-beam) Lithography: Patterning experiments on Si wafer substrates were conducted in the University of Maryland's FabLab on a Raith e-line EBL system operating at acceleration voltages between 5-30 kV with a 30-µm aperture size for 5 kV and a 20-µm aperture size for 20 and 30 kV resulting in currents of 179.3, 149.8, and 163.6 pA for 5, 20, and 30 kV, respectively. The desired doses were set, and the corresponding dwell times were calculated in the Raith e-line software based on the dose and current. Pattern files were generated in Raith's patterning software and were exported as GDS files. Patterning experiments on SiNx TEM substrates were conducted on a ThermoFisher Helios G4 UC Focused Ion Dual Beam Microscope. A desired acceleration voltage between 2-30 kV was chosen and a beam current of 100 pA was used. All patterns were exposed for a dwell time of 1 µs while the pass (scan) number was varied in each exposure to obtain the desired electron dose. The electron dose was calculated as a function of the pixel size, the current, number of scans, and the dwell time. Pattern files were generated in Adobe Photoshop with a pixel density of 454 pixels per inch and a pixel size of 2.1 nm. Patterning at 100 keV was performed at Brookhaven National Lab's Center for Functional Nanomaterials on a JEOL JBX6300-FS electron beam lithography tool using a beam current of approximately 1 nA with doses ranging from 10,000 to 200,000 µC cm^{-2}.

Line Edge Roughness (LER) and Line Width Roughness (LWR) Measurements: LER and LWR were calculated using SuMMIT™ (EUV Technology) image analysis software. AFM images with high contrast between irradiated and non-irradiated areas were fed into the software. For measurements on a Si substrate, an AFM image (2.37 nm $pixel^{-1}$) of 50 nm pitch lines was used and values were extracted as the average of 5 lines.

Electron Beam Irradiation for Full Wafer Characterization: Irradiation of entire aZnMIm-coated wafers for characterization was performed in a home-built UHV system equipped with an electron gun (ELG-2, Kimball Physics). Samples were loaded into the UHV chamber until the pressure was below 5 x 10^{-8} Torr. Chamber pressure was kept below 1 × 10^{-7} Torr during irradiation. Beam parameters were controlled by the electron gun power supply unit (EGPS-1022, Kimball Physics). The electron energy for all experiments was 2 keV with an emission current of 4 µA, corresponding to an approximate electron flux of 1.3 µA cm^{-2} for a circular irradiation area with 2 cm diameter. Positioning of samples in the irradiation area was confirmed by phosphor coated Si wafers on the sample holder.

Dry Deposition of Amorphous Zinc-Imidazolate Thin Films by Atomic/Molecular Layer Deposition (ALD/MLD): Silicon (111) wafers to be used as substrates were cut into 1 x 1 cm pieces and cleaned by

sonication in ethanol for 15 s. The native SiO_2 film thickness was measured by ellipsometry, and substrates with an oxide film thickness of greater than 2.1 nm were not used. Silicon nitride (SiNx) TEM supports were treated in an O_2 plasma cleaner for 2 minutes before deposition. Au-coated Si (100) wafers used for IRRAS were cut into 1 x 1 cm pieces and used without further cleaning. DEZ and 2MIm were pulsed sequentially into a home-built flow-through ALD reactor (Figure S1) with intermittent Ar gas purges to remove byproducts and unreacted precursors. The DEZ precursor cylinder was maintained at ambient temperature, and the 2MIm precursor cylinder was placed in a box oven with the reactor, as shown in Figure S1. Pulse lengths of DEZ and 2MIm were fixed at 50 ms and 100 ms, respectively. Purge lengths of 30 s for DEZ and 45 s for 2MIm were used. Reactor temperatures of 100 – 175 °C were tested. The precursor inlet and reactor outlet lines were heated to 150 °C to prevent condensation of 2MIm and DEZ. The Ar flow rate in the reactor was set to 10 sccm and the reactor pressure was 0.3 – 1.5 mbar during the deposition (Figure S2a). See Figure S1 for a schematic and images of the deposition system.

Preparation of ZnO-ZIF-8 Films for Comparative IRRAS Analysis: Silicon (111) wafers were prepared in the same manner as described above for the aZnMIm films. ZnO films of 12 nm thickness were deposited in 100 cycles of alternating 15 ms pulses of H_2O (Milli-Q) and DEZ (Strem) precursors separated by 5 s N_2 purges at 125 °C in a commercial Veeco Savannah S200 ALD reactor. The ZnO films were placed on a stainless-steel mesh in a quartz tube with 2MIm (100 mg, 1.22 mmol) and heated to 120 °C for two hours at a base pressure of 5 x 10^{-2} mbar to convert them to ZnO-ZIF-8. After conversion, the films were activated at 120 °C in a clean quartz tube for one hour under dynamic vacuum.

Preparation of aZnMIm-ZIF-8 Films for IR and XRD Analysis: aZnMIm films of 60 nm thickness were deposited on Au-coated Si wafers (for IRRAS) and Silicon (111) wafers (for XRD) in 400 ALD/MLD cycles using a sequence of **(1)** 50 ms DEZ pulse, **(2)** 30 s Ar purge, **(3)** 100 ms 2MIm pulse, **(4)** 45 s Ar purge. The aZnMIm films were placed on a stainless-steel mesh in a quartz tube with 2MIm (100 mg, 1.22 mmol) and heated to 60, 80, 100, or 120 °C for 30 minutes, one hour, two hours, or four hours at a base pressure of 5 x 10^{-2} mbar to convert them to ZnO-ZIF-8. After conversion, the films were activated at 120 °C in a clean quartz tube for one hour under dynamic vacuum.

Dry Etching: Films were placed in a cylindrical quartz reactor and transferred to an oven. The system was heated to 120 °C under dynamic vacuum with an imposed 5 sccm argon flow at a pressure of 2 mbar and evacuated for 30 minutes. For a single treatment cycle, the hfacH valve was opened for 2 s and the sample was exposed to a static hfacH pressure of 6.5 mbar for 5 minutes before being purged by dynamic vacuum with argon flow for 5 minutes at a pressure of 2 mbar followed by a dynamic vacuum purge without argon flow for 1 minute. Samples were treated for 1 to 10 treatment cycles (6 cycles for patterned samples). Following treatment, the system was evacuated under dynamic vacuum with argon flow for 30 minutes at 120 °C.

Conflicts of Interest

The authors declare no competing financial interests.

Acknowledgments

E-beam patterning and etching experiments were supported by the Semiconductor Research Corporation (SRC) contract No 2022-NM-3114. ALD/MLD experiments and IRAAS characterization were supported by the U.S. Department of Energy, Office of Science, Office of Basic Energy Sciences, Division of Chemical Sciences, Geosciences, and Biosciences under award DE-SC0021212 and award DE-SC0021304, respectively. This research used the JEOL JBX6300-FS Electron Beam Lithography Tool of the Center for Functional Nanomaterials (CFN), which is a U.S. Department of Energy Office of Science User Facility, at Brookhaven National Laboratory under Contract No. DE-SC0012704. Part of the spectroscopy characterization work was carried out at the Center for Functional Nanomaterials at

Brookhaven National Laboratory, supported by the U.S. Department of Energy, Office of Basic Energy Sciences, under Contract No. DE-SC0012704. This work was performed (in part) at the Materials Characterization and Processing Center in the Whiting School of Engineering at Johns Hopkins University. The authors would like to thank Jonathan Hummel and the staff at the University of Maryland Nanocenter Fabrication Laboratory (FabLab) for their help with electron beam lithography techniques. The authors are grateful to the Morgan State University (MSU) Department of Physics and Engineering Physics for the use of their TEM and microscopy/microanalysis facilities. The MSU JEOL TEM was supported by the National Institute on Minority Health and Health Disparities through grant number 5U54MD013376 and National Institute of General Medical Sciences through grant number 5UL1GM118973. P.C., K.E.W., and P.M.E. contributed equally to this work. M.T. and D.H.F. contributed equally to this work.

Funding Statement

E-beam patterning and etching experiments were supported by the Semiconductor Research Corporation (SRC) contract No 2022-NM-3114. ALD/MLD experiments and IRAAS characterization were supported by the U.S. Department of Energy, Office of Science, Office of Basic Energy Sciences, Division of Chemical Sciences, Geosciences, and Biosciences under award DE-SC0021212 and award DE-SC0021304, respectively. This research used the JEOL JBX6300-FS Electron Beam Lithography Tool of the Center for Functional Nanomaterials (CFN), which is a U.S. Department of Energy Office of Science User Facility, at Brookhaven National Laboratory under Contract No. DE-SC0012704. Part of the spectroscopy characterization work was carried out at the Center for Functional Nanomaterials at Brookhaven National Laboratory, supported by the U.S. Department of Energy, Office of Basic Energy Sciences, under Contract No. DE-SC0012704. The MSU JEOL TEM was supported by the National Institute on Minority Health and Health Disparities through grant number 5U54MD013376 and National Institute of General Medical Sciences through grant number 5UL1GM118973.

References

[1] P. J. Silverman, *J Microlith Microfab* **2005**, 4, 011006.
[2] B. Wu, A. Kumar, *J. Vac. Sci. Technol., B: Microelectron. Nanometer Struct.--Process., Meas., Phenom.* **2007**, 25, 1743-1761.
[3] R. S. Wise, Proc. SPIE 11612, Advances in Patterning Materials and Processes XXXVIII, 1161203, **2021**.
[4] B. Volosskiy, T. W. Weidman, S. S. Tan, C. Wu, K. Gu, (LAM Research Corporation) World Patent WO2020132281A1, **2020**.
[5] P. Sundberg, M. Karppinen, *Beilstein J. Nanotechnol.* **2014**, *5*, 1104-1136.
[6] I. Stassen, M. Styles, G. Grenci, H. V. Gorp, W. Vanderlinden, S. D. Feyter, P. Falcaro, D. D. Vos, P. Vereecken, R. Ameloot, *Nat. Mater.* **2016**, *15*, 304-310.
[7] J. Smets, A. J. Cruz, V. Rubio-Giménez, M. L. Tietze, D. E. Kravchenko, G. Arnauts, A. Matavž, N. Wauteraerts, M. Tu, K. Marcoen, I. Imaz, D. Maspoch, M. Korytov, P. M. Vereecken, S. De Feyter, T. Hauffman, R. Ameloot, *Chem. Mater.* **2023**, *35*, 1684-1690.
[8] S. M. George, B. Yoon, A. A. Dameron, *Acc. Chem. Res.* **2009**, *42*, 498-508.
[9] E. Ahvenniemi, M. Karppinen, *Chem. Commun.* **2016**, *52*, 1139-1142.
[10] E. Ahvenniemi, M. Karppinen, *Chem. Mater.* **2016**, *28*, 6260-6265.
[11] L. D. Salmi, M. J. Heikkilä, E. Puukilainen, T. Sajavaara, D. Grosso, M. Ritala, *Microporous Mesoporous Mater.* **2013**, *182*, 147-154.
[12] K. B. Lausund, O. Nilsen, *Nat. Commun.* **2016**, *7*, 13578.
[13] J. Shi, A. Ravi, N. E. Richey, H. Gong, S. F. Bent, *ACS Appl. Mater. Interfaces* **2022**, *14*, 27140-27148.
[14] S. K. Tero, V. Michaela, E. Yasin, Proc. SPIE 9776, Extreme Ultraviolet (EUV) Lithography VII, 97762N, **2016**.
[15] S. J. Pearton, R. J. Shul, F. Ren, *MRS Internet Journal of Nitride Semiconductor Research* **2000**, *5*, e11.
[16] F. Rousseau, A. Jain, T. T. Kodas, M. Hampden-Smith, J. D. Farr, R. Muenchausen, *J. Mater. Chem.* **1992**, *2*, 893-894.
[17] S. R. Droes, T. T. Kodas, M. J. Hampden-Smith, *Adv. Mater.* **1998**, *10*, 1129-1133.
[18] D. Dictus, C. Wu, E. C. Hansen, T. W. Weidman (LAM Research Corporation) World Patent WO 2022125388A1, **2022**.
[19] T. W. Weidman, K. L. Nardi, D. Dictus, B. Kam, C. Wu, E. C. Hansen, N. Kenane, K. L. Gu (LAM Research Corporation) World Patent WO WO2021072042A1, **2021**.
[20] H. Xu, K. Sakai, K. Kasahara, V. Kosma, K. Yang, H. C. Herbol, J. Odent, P. Clancy, E. P. Giannelis, C. K. Ober, *Chem. Mater.* **2018**, *30*, 4124-4133.
[21] K. S. Park, Z. Ni, A. P. Cote, J. Y. Choi, R. D. Huang, F. J. Uribe-Romo, H. K. Chae, M. O'Keeffe, O. M. Yaghi, *Proc. Natl. Acad. Sci. U.S.A.* **2006**, *103*, 10186-10191.
[22] M. Tu, B. Xia, D. E. Kravchenko, M. L. Tietze, A. J. Cruz, I. Stassen, T. Hauffman, J. Teyssandier, S. De Feyter, Z. Wang, R. A. Fischer, B. Marmiroli, H. Amenitsch, A. Torvisco, M. d. J. Velásquez-Hernández, P. Falcaro, R. Ameloot, *Nat. Mater.* **2021**, *20*, 93-99.
[23] K. Noh, J. Lee, J. Kim, *Isr. J. Chem.* **2018**, *58*, 1075-1088.
[24] O. Karagiaridi, M. B. Lalonde, W. Bury, A. A. Sarjeant, O. K. Farha, J. T. Hupp, *J. Am. Chem. Soc.* **2012**, *134*, 18790-18796.
[25] M. Tu, H. Reinsch, S. Rodríguez-Hermida, R. Verbeke, T. Stassin, W. Egger, M. Dickmann, B. Dieu, J. Hofkens, I. F. J. Vankelecom, N. Stock, R. Ameloot, *Angew. Chem. Int. Ed. Engl.* **2019**, *58*, 2423.
[26] S. Conrad, P. Kumar, F. Xue, L. Ren, S. Henning, C. Xiao, K. A. Mkhoyan, M. Tsapatsis, *Angew. Chem. Int. Ed. Engl.* **2018**, *57*, 13592-13597.
[27] M. Krishtab, I. Stassen, T. Stassin, A. J. Cruz, O. O. Okudur, S. Armini, C. Wilson, S. De Gendt, R. Ameloot, *Nat. Commun.* **2019**, *10*, 3729.

[28] Y. Miao, D. T. Lee, M. D. de Mello, M. Ahmad, M. K. Abdel-Rahman, P. M. Eckhert, J. A. Boscoboinik, D. H. Fairbrother, M. Tsapatsis, *Nat. Commun.* **2022**, *13*, 420.
[29] Y. Miao, M. Tsapatsis, *Chem. Mater.* **2021**, *33*, 754-760.
[30] Q. Liu, Miao, Y., Villalobos, L. F., Li, S., Babu, D. J., Chen, C., Chi, H.-Y., Vahdat, M. T., Hao, J., Song, S., Han, Y., Tsapatsis, M., & Agrawal, K. V., *Nat. Mater. (Accepted)* **2023**.
[31] A. Chaker, H. A. Alty, P. Winpenny, G. F. S. Whitehead, G. A. Timco, S. M. Lewis, R. E. P. Winpenny, *ACS Appl. Nano. Mater.* **2022**, *5*, 17538-17543.
[32] S. L. Wood, G.; Metzler, M., Quattrone Nanofabrication Facility, **2016**, 1.
[33] J.-K. Huang, N. Saito, Y. Cai, Y. Wan, C.-C. Cheng, M. Li, J. Shi, K. Tamada, V. C. Tung, S. Li, L.-J. Li, *ACS Mater. Lett.* **2020**, *2*, 485-491.
[34] J. López-Cabrelles, J. Romero, G. Abellán, M. Giménez-Marqués, M. Palomino, S. Valencia, F. Rey, G. Mínguez Espallargas, *J. Am. Chem. Soc.* **2019**, *141*, 7173-7180.
[35] M. Hayashi, D. T. Lee, M. D. de Mello, J. A. Boscoboinik, M. Tsapatsis, *Angew. Chem. Int. Ed. Engl.* **2021**, *60*, 9316-9320.
[36] C. N. Eads, J.-Q. Zhong, D. Kim, N. Akter, Z. Chen, A. M. Norton, V. Lee, J. A. Kelber, M. Tsapatsis, J. A. Boscoboinik, J. T. Sadowski, P. Zahl, X. Tong, D. J. Stacchiola, A. R. Head, S. A. Tenney, *AIP Adv.* **2020**, *10*, 085109.
[37] F. Menges "Spectragryph - optical spectroscopy software", Version 1.2.16.1, 2022, http://www.effemm2.de/spectragryph/.
[38] T. T. Weng, J. R. Schmidt, *J. Phys. Chem. C* **2020**, *124*, 1458-1468.
[39] F. Tian, A. Cerro, A. Mosier, H. Wayment-Steele, R. Shine, A. Park, E. Webster, L. Johnson, M. Johal, L. Benz, *J. Phys. Chem. C* **2014**, *118*, 14449-14456.
[40] C. Chizallet, N. Bats, *J. Phys. Chem. Lett* **2010**, *1*, 349-353.
[41] W. Zhou, J. Leem, I. Park, Y. Li, Z. Jin, Y. S. Min, *J. Mater. Chem.* **2012**, *22*, 23935-23943.
[42] B. Xu, Y. Mei, Z. Xiao, Z. Kang, R. Wang, D. Sun, *Phys. Chem. Chem. Phys.* **2017**, *19*, 27178.
[43] Y. Zhang, Y. Jia, L. a. Hou, *RSC Adv.* **2018**, *8*, 31471-31477.
[44] A. J. Cruz, I. Stassen, M. Krishtab, K. Marcoen, T. Stassin, S. Rodríguez Hermida, J. Teyssandier, S. Pletincx, R. Verbeke, V. Rubio-Giménez, S. Tatay, C. Martí-Gastaldo, J. Meersschaut, P. Vereecken, S. Feyter, T. Hauffman, R. Ameloot, *Chem. Mater.* **2019**, *31*, 9462-9471.
[45] M. Dorneles de Mello, M. Ahmad, D. T. Lee, P. Dimitrakellis, Y. Miao, W. Zheng, D. Nykypanchuk, D. G. Vlachos, M. Tsapatsis, J. A. Boscoboinik, *ACS Appl. Mater. Interfaces* **2022**, *14*, 19023-19030.
[46] H. Miyoshi, J. Taniguchi, *J. Vac. Sci. Technol. B. Nanotechnol. Microelectron.* **2015**, *33*, 06FD05.
[47] C. Fang, Y. Cao, D. Wu, A. Li, *Prog. Nat. Sci.: Mater. Int.* **2018**, *28*, 667-675.
[48] A. H. Basher, I. Hamada, S. Hamaguchi, *Jpn. J. Appl. Phys.* **2020**, *59*, 090905.
[49] H. Kung, A. Teplyakov, *J. Catal.* **2015**, *330*, 145-153.
[50] G. Distefano, M. Guerra, D. Jones, A. Modelli, *Spectrochim. Acta, Part A* **1982**, *38*, 85-89.
[51] J. Wnuk, J. Gorham, D. Fairbrother, *J. Phys. Chem. C.* **2009**, *113*, 12345-12354.
[52] R. Meißner, L. Feketeová, A. Ribar, K. Fink, P. Limão-Vieira, S. Denifl, *J. Am. Soc. Mass Spectrom.* **2019**, *30*, 2678-2691.
[53] R. N. Widmer, G. I. Lampronti, N. Casati, S. Farsang, T. D. Bennett, S. A. T. Redfern, *Phys. Chem. Chem. Phys.* **2019**, *21*, 12389-12395.
[54] S. Ghosh, H. Yun, P. Kumar, S. Conrad, M. Tsapatsis, K. A. Mkhoyan, *Chem. Mater.* **2021**, *33*, 5681.
[55] T. G. Oyama, A. Oshima, S. Tagawa, *AIP Adv.* **2016**, *6,* 085210.
[56] S. Lewis, G. Derose, H. Alty, M. Hunt, N. Lee, J. Mann, R. Grindell, A. Wertheim, L. de Rose, A. Fernandez Mato, C. Muryn, G. Whitehead, G. Timco, A. Scherer, R. Winpenny, *Adv. Funct. Mater.* **2022**, *32,* 2202710.

[57] S.-W. Nam, M. Rooks, J. Yang, K. Berggren, H.-M. Kim, M.-H. Lee, K.-B. Kim, J. H. Sim, D. Yoon, *J. Vac. Sci. Technol. B* **2009**, *27*, 2635-2639.
[58] M. S. M. Saifullah, M. Asbahi, M. Binti-Kamran Kiyani, S. Tripathy, E. A. H. Ong, A. Ibn Saifullah, H. R. Tan, T. Dutta, R. Ganesan, S. Valiyaveettil, K. S. L. Chong, *ACS Nano* **2017**, 11, 9920-9929.
[59] M. Saifullah, S. K.R.V, D. Anderson, D. J. Kang, W. Huck, G. Jones, M. Welland, *J. Vac. Sci. Technol. B* **2006**, *24*, 1215-128.
[60] J. Zhang, K. Cao, X. S. Wang, B. Cui, *Chem. Commun.* **2015**, *51*, 17592-17595.
[61] K. Fairley, M. Sharps Noyes, G. Mitchson, J. Ditto, D. Johnson, D. Johnson, *J. Vac. Sci. Technol., B: Nanotechnol. Microelectron.: Mater., Process., Meas., Phenom.* **2016**, *34*, 041607.
[62] J. Peter, M. Moinuddin, S. Ghosh, S. Sharma, K. Gonsalves, *ACS Appl. Polym. Mater.* **2020**, *2*, 1790-1799.
[63] H. Wang, X. Pei, M. J. Kalmutzki, J. Yang, O. M. Yaghi, *Acc. Chem. Res.* **2022**, *55*, 707-721.
[64] S. O. Kim, D. C. Lee, *Surf. Coat. Technol.* **1999**, *120-121*, 746-751.
[65] Y. Mao, N. M. Felix, P. T. Nguyen, C. K. Ober, K. K. Gleason, *J. Vac. Sci. Technol. B* **2004**, *22*, 2473-2478.
[66] F. Pfeiffer, C. Neuber, H.-W. Schmidt, *Proc. SPIE* **2008**, 6923, 69231F.
[67] D. Le, T. Park, S. M. Hwang, J. Kim, Y. C. Jung, N. Tiwale, A. Subramanian, W.-I. Lee, R. Choi, M. Sung, C.-Y. Nam, J. Kim, *Jpn. J. Appl. Phys.* **2023**, *62*, SG0812.

Table of Contents

A solvent-free deposition and patterning process has been developed using an inorganic-organic hybrid material comprised of Zn^{2+} and 2-methylimidazolate linkers deposited by atomic/molecular layer deposition (ALD/MLD) to yield smooth, amorphous resist films. Using electron beam lithography (EBL), linewidths of 22 nm have been achieved using the vapor phase etchant 1,1,1,5,5,5-hexafluoroacetylacetone (hfacH) at 120 °C.

Zinc-Imidazolate Films as an All-Dry Resist Technology

*Peter Corkery †, Kayley E. Waltz †, Patrick M. Eckhert †, Mueed Ahmad, Andrea Kraetz, Yurun Miao, Dennis T. Lee, Mohammed K. Abdel-Rahman, Yucheng Lan, Paul Haghi-Ashtiani, Aaron Stein, J. Anibal Boscoboinik, Michael Tsapatsis * & D. Howard Fairbrother **